

Effects of the scalar parameters in the Suzen-Huang model on plasma actuator characteristics

I.H. Ibrahim¹, M. Skote*¹

¹School of Mechanical & Aerospace Engineering, Nanyang Technological University, 50 Nanyang Avenue, Singapore 639798
Tel: +6567904271/ FAX: +6567924062

*Corresponding author. Email: mskote@ntu.edu.sg

1. ABSTRACT

For the past decade, plasma actuators have been identified as a subset in the realm of active flow control devices. As research into plasma actuators continues to mature, computational modelling is needed to complement the investigation of the actuators. In this study, the Suzen-Huang model is chosen because of its ability to simulate both the charge density and Lorentz body force. Its advantages and limitations have been identified with a parametric study of two constants used in the modelling; the Debye length and the maximum charge density. By varying the two scalars, the effects on charge density, body force and induced velocity are examined. By the definition of the Lorentz body force, a linear relationship can be deduced between the non-dimensionalised body force and maximum charge density. However, results show that the non-dimensionalised body force is nonlinearly dependent on Debye length. The optimized form of the Suzen-Huang model shows better agreement in the horizontal velocity profile but still points to inaccuracy when compared to vertical velocity profile. The results indicate that the body force still has to be modelled more extensively above the encapsulated electrode, so that the horizontal and vertical components of induced velocities are accurately obtained.

Keywords: plasma actuator, computational modelling, Debye length, charge density

2. INTRODUCTION

The earliest design of plasma actuators for flow control evolved from the investigations of paraelectric forces by Roth (1998) in the One Atmospheric Uniform Glow Discharge Plasma (OAUGDPTM) design. Paraelectricity refers to the ability of a material to become polarized in an applied electric field. When the air is polarized, mobile ions collide and transfer momentum to the heavier neutral molecules. This results in the induced fluid motion which is described as a plasma actuation.

The novelty of the flow control method is that it allows selective injection of body force into a neutral fluid without the use of mechanical flaps or other excitation methods. A tilted-plate plasma reactor that results in an unstable equilibrium due to paraelectric body forces was designed in Roth et al. (1998). The body forces are formed as a result of the collision of the ions and neutral molecules. This is the basis of the plasma actuator which results in momentum transfer of charged to neutral particles, inducing airflow. The general aspects of the design include a DC high voltage power supply and an asymmetrical placement of the cathode and anode sources. Once the voltage supply has been powered, the gases between the two electrodes are ionized to become plasma. The design of the tilted electrodes results in the motion of the ionized particles, producing plasma convection. By varying the positions of the electrodes and inserting a dielectric surface, a more stable plasma discharge is formed. This subsequently led to the design shown in Figure 1. The single asymmetric electrodes can be placed in an array to produce higher induced velocities. In a later investigation by Roth (2001), he predicted that the array design would be able to produce an induced velocity of up to 100 m/s. However, we acknowledge that there has not been any experiment data to verify his model prediction. The single asymmetric electrode shown in (a) of Figure 1 is further investigated by (Orlov (2006); Orlov et al. (2007)) and (Corke et al. (2008); Corke et al. (2009)). The Single Dielectric Barrier Discharge (SDBD) consists of one electrode exposed to the surrounding air and one electrode completely encapsulated by a dielectric material. This results in an asymmetric geometry. An alternating current (AC) voltage is supplied to power the actuator. The

asymmetric electrode design results in a body force that induces the flow in the direction from the exposed electrode toward the covered electrode. The geometry of the SDBD is shown in Figure 2.

The mechanism of adding momentum to the fluid is as follows: upon activating the AC voltage source, plasma appears on the insulator surface above the insulated electrode. Directed momentum, coupled with the surrounding air, substantially affects the airflow. The plasma is formed as a result of a series of plasma discharges as electrons are transferred onto and off of the dielectric surface. The process is self limiting because the electrons emitted from the exposed electrode collect on the dielectric surface, are returning during the subsequent half-cycle of the plasma discharge. These emitted electrons ionize the neutral molecules, creating both positive and negative ions. Further collisions of the ions into neutral molecules induce motion to the gas. The plasma sweep depends on the frequency and amplitude of voltage waveform change. More factors will be discussed in later sections of this paper.

In the next section, an introduction to the computational model is given together with a description of the purpose of the current paper.

A. COMPUTATIONAL MODELS

The multitude of parameters involved in the design of the plasma actuator points to the use of CFD as a tool in the design process. Experimental methods pose a disadvantage because it results in high costs when designing actual geometries and data. The computational models have evolved from the late 1990s till today. Generally, all computational models require a coupling of the ‘plasma’ equations with the ‘flow’ equations. The Lorentz force is used to couple the resultant force produced by the charges to the source terms in the Navier-Stokes equations. Two forms of modelling the plasma actuator can be derived from the existing modelling techniques: the microscopic (Massines et al. (1998); Boeuf et al. (2005); Rouffet (2008)) and macroscopic form (Roth et al. (1998); Orlov et al. (2005); Suzen et al. (2005)). The microscopic model captures the motion of the charge particles by coupling the drift-diffusion equation with the Maxwell equation. The time scale defining a microscopic plasma process is about 10^{-8} to 10^{-9} s, which is in the same order of the mobility of charged particles. The macroscopic form captures the essential physics of the flow by modelling the electric potential characteristics as well as defining the charge density that forms the Lorentz body force. The time scale involved in this process is normally about 10^{-4} s, which is defined by the frequency of the AC voltage required to power the actuator. The length scale for both the microscopic and macroscopic forms are obtained from the Debye lengths of the simulation, which is about 10^{-4} m.

One of the earlier microscopic plasma modelling was conducted by Massines et al. (1998). It consists of a one-dimensional model based on simultaneous solution of continuity equations for charged and excited particles and the Maxwell equation. The use of these equations laid the foundation for future microscopic models. The study conducted by Boeuf et al. (2005) considered nitrogen and oxygen at atmospheric pressure. The model includes other complicated gas chemistry which has 230 reaction equations. A study by Rouffet (2008) consists of a mixture of ions, electrons and neutral molecules. The model is made up of the drift-diffusion and the Maxwell equation (Gauss’s law) for the electrons and ions as shown below:

$$\frac{\partial n_e}{\partial t} + \nabla \cdot [-n_e \mu_e \mathbf{E} - D_e \nabla n_e] = n_e v_i - r n_e n_i \quad (1)$$

$$\frac{\partial n_i}{\partial x} + \nabla \cdot [n_i \mu_i \mathbf{E} - D_i \nabla n_i] = n_e v_i - r n_e n_i \quad (2)$$

$$\nabla \cdot (\epsilon \mathbf{E}) = \frac{e}{\epsilon_0} (n_i - n_e) \quad (3)$$

$$\mathbf{F}_b = \rho_c \mathbf{E} = e(n_i - n_e) \nabla \phi \quad (4)$$

where \mathbf{F}_b is the Lorentz Body Force (N/m^3), n_e and n_i are electron and ion densities ($1/\text{m}^3$), μ_e and μ_i are electro and ion mobility ($\text{m}^2/(\text{sV})$), \mathbf{E} is the electric field (V/m), D_e and D_i are diffusion coefficients, ν_i is the ionisation frequency ($1/\text{s}$), r is the recombination rate, (m^3/s), ϵ_0 is the vacuum permittivity (F/m), ϵ is the relative permittivity, and e is the electron charge (C), ρ_c is the charge density (C/m^3) and ϕ is the electrical potential.

The influence on airflow due to the body force is accounted for by including the body force in the Navier-Stokes equations:

$$\rho \frac{\partial \mathbf{u}}{\partial t} + \nabla(\eta \nabla \mathbf{u}) + \rho(\mathbf{u} \cdot \nabla) \mathbf{u} + \nabla p = e(n_i - n_e) \nabla \phi$$

$$\nabla \cdot \mathbf{u} = 0$$
(5)

Another approach to modelling the body force of the plasma actuator is through time-averaging, as done by Roy et al. (2008). The first-principle based electrohydrodynamic force modelling technique used in their studies is basically an average solution obtained from a micro-actuator modelling technique Singh et al. (2005) mentioned in our study.

The first macroscopic model was done by Roth et al. (1998) who coined the paraelectric and peristaltic (OAUGDPTM) forms of DBD actuator. Their team used a simple method to calculate body force which is proportional to the squared electric field and the vacuum permittivity. Equation (6) shows this relation:

$$\mathbf{F}_b = \frac{1}{2}(\epsilon_0 \mathbf{E}^2)$$
(6)

Further analysis by Enloe et al. (2004b) shows that there is an inaccuracy in the body force estimation made by Roth. The assumption made for the gradient of the electric field was for one-dimensional flow and rests on the assertion that

$$\nabla \mathbf{E}^2 = 2\mathbf{E}(\nabla \cdot \mathbf{E})$$
(7)

which is true only for a one-dimensional flow which does not apply for the aerodynamic plasma actuator.

A later model that does not use this assumption and is derived based on the relations of the species charged densities with the Boltzmann equation and temperature with the Debye length variables was introduced by Orlov et al. (2005). The model concludes that the net charge density at any point in the plasma is proportional to the potential at that point and is written as:

$$\mathbf{F}_b = \rho_c \mathbf{E} = -\left(\frac{\epsilon_0}{\lambda_D^2}\right) \Phi \mathbf{E}$$
(8)

Finally, the plasma actuator model designed by Suzen et al. (2005) studies the implication of splitting the total electric potential term (Φ) into two parts: one being influenced by external electric field (ϕ), and the other potential affected by the net charge density (φ).

$$\Phi = \phi + \varphi$$
(9)

$$\nabla \cdot (\epsilon_r \nabla \phi) = 0$$
(10)

$$\nabla \cdot (\epsilon_r \nabla \varphi) = \rho_c / \epsilon_0$$
(11)

$$\mathbf{F}_b = \rho_c (-\nabla \phi)$$

(12)

This technique has been applied to the design of turbine blades (Suzen et al. (2005); Suzen et al. (2006); Reasor Jr et al. (2007); Suzen et al. (2007)) to achieve reduction in flow separation. The modelling allows the representation of the charge density on the top of the encapsulated electrode to be controlled. The presence of this feature shows good potential in providing an idealized model which encompasses both microscopic and macroscopic plasma actuator modelling characteristics.

The microscopic (or charge transport) models solve for the trajectories of the individual charge particles that constitutes the charge density. This type of model requires high computing resources compared to the macroscopic S-H model which solves the charge density as a single entity. In addition, since the model is originally defined for a flow control study, detailed evolutionary aspects of the charge density term is not as important as determining the final induced velocities of the plasma actuator. In the S-H model, the charge density is one of the two variables that define the body force term, the other being the electric field strength. Visualizing the growth of the charge density would allow investigators to understand the relationship between the charge density and the body force/ induced velocity (see further in Section 5B and 5C).

The purpose of this paper is to conduct substantial analysis of the Suzen-Huang model by parametrically changing two scalar variables that are inherent in the model. The two variables are the Debye Length and Maximum Charge Density. These terms could be used as model calibrating tools that will affect the surface charge propagation on the dielectric surface, thereby influencing body force and induced velocity. Previous studies (Suzen et al. (2005); Suzen et al. (2006); Reasor Jr et al. (2007); Suzen et al. (2007)) have only concluded these effects qualitatively. Our study aims to quantitatively describe these changes in both area and magnitude, and investigate the effects on body force and induced velocity.

3. DETAILS OF THE SUZEN-HUANG MODEL

The design of the Suzen-Huang plasma actuator model has its roots in the concept of electroosmotic flow introduced by Henry (1931). Electroosmotic flow refers to the motion of fluid induced by the presence of an applied voltage in a capillary tube or narrow channel. Since the Debye length used in the plasma actuators is small, the motion of the charged particles is similar to electroosmotic flow. The mathematical equation describing the flow is based on the division of the electric potential into two parts: one from the external electric field and the other from the surface of the walls. By coupling the body force obtained from the electromagnetic equation to the Navier-Stokes equations, modelling of the plasma actuator can be conducted.

In the next section, the governing equations and boundary conditions for the plasma domain will be formulated as introduced in Suzen et al. (2005). The equation for the plasma body force will then be derived based on the solution of the electrostatics. Finally, the equations for the flow problem will be presented.

A. GOVERNING EQUATIONS AND BOUNDARY CONDITIONS

The steady-state incompressible Navier Stokes equation can be solved in COMSOL (2008) via the momentum and continuity equations shown:

$$\begin{aligned}\rho(\mathbf{u} \cdot \nabla)\mathbf{u} - \eta \nabla^2 \mathbf{u} + \nabla p &= \mathbf{F}_b \\ \nabla \cdot \mathbf{u} &= 0\end{aligned}\tag{13}$$

where ρ refers to density (1.2 kg/m^3), \mathbf{u} is the velocity (m/s), η is the dynamic viscosity ($1.8 \times 10^{-5} \text{ kg/ms}$), p is pressure (Pa) and \mathbf{F}_b is the Lorentz body force (N/m^3).

The body force is calculated from the Lorentz equation which can be written as:

$$\mathbf{F}_b = \rho_c (\mathbf{E} + \mathbf{u} \times \mathbf{B})\tag{14}$$

where ρ_c is the charge density (C/m^3), \mathbf{E} is the electric field (V/m) and \mathbf{B} is the magnetic field (T).

The Lorentz equation is derived from the generic Maxwell equations which describes electromagnetic phenomena (Davidson (2001)). Individually, the Maxwell equations are known as Gauss's law, Gauss's law for magnetism, Faraday's law of induction, and Ampere's law with Maxwell's correction. Written in free charge and current, and in differential form, they are:

$$\begin{aligned} \nabla \cdot \mathbf{D} &= \rho_c \\ \text{(Gauss's Law)} \end{aligned} \tag{15}$$

$$\begin{aligned} \nabla \cdot \mathbf{B} &= 0 \\ \text{(Gauss's Law for Magnetism)} \end{aligned} \tag{16}$$

$$\begin{aligned} \nabla \times \mathbf{E} &= -\frac{\partial \mathbf{B}}{\partial t} \\ \text{(Faraday's Law of Induction)} \end{aligned} \tag{17}$$

$$\begin{aligned} \nabla \times \mathbf{H} &= \mathbf{J}_f + \frac{\partial \mathbf{D}}{\partial t} \\ \text{(Ampere's law with Maxwell's correction)} \end{aligned} \tag{18}$$

where \mathbf{D} is the induced electric field (V/m), \mathbf{B} is the magnetic field (T), \mathbf{E} is the electric field (V/m), \mathbf{H} is the induced magnetic field (T) and \mathbf{J}_f is the induced current (A/m).

The system is taken as quasi-steady because of the nature of plasma formation and its overall effect to the fluid system. The AC period is long (10^{-4} s) compared to the time needed for the charges in the plasma to redistribute (10^{-8} s- 10^{-9} s) so that the system is quasi steady. Similar modelling assumptions have been made in Orlov et al. (2006); Orlov et al. (2007) and Jayaraman et al. (2007).

In the case of a quasi-steady system, \mathbf{J}_f , \mathbf{B} and \mathbf{H} are equal to zero. In addition, the time derivatives $\partial \mathbf{B} / \partial t$ and $\partial \mathbf{D} / \partial t$ also equals to zero. Hence only Gauss's law remains.

The electric induction is related to the electrical field strength via:

$$\mathbf{D} = \varepsilon \mathbf{E} \tag{19}$$

where ε is the dielectric coefficient (F/m). The term ε can be written as $\varepsilon = \varepsilon_0 \varepsilon_r$, where ε_r refers to the relative permittivity of a medium and ε_0 is the vacuum permittivity (8.85×10^{-12} F/m).

Also, the electric field is related to the electric potential Φ , via:

$$\mathbf{E} = -\nabla \Phi \tag{20}$$

The Lorentz body force is now simplified from Equation (14) and can be written as:

$$\mathbf{F}_b = \rho_c \mathbf{E} = \rho_c (-\nabla \Phi) \tag{21}$$

The resulting Equation (21) will be further simplified later.

Next, substituting equations (19) and (20) into (15), we obtain:

$$\nabla \cdot (\varepsilon_r \nabla \Phi) = \rho_c / \varepsilon_0 \tag{22}$$

which constitutes the relation between the two variables Φ and ρ_c .

B. DEBYE LENGTH

To proceed from here, we need one more equation relating these two quantities, which can be found via the Debye length, λ_D . Essentially, the Debye length determines whether body forces come into play or not. Oppositely charged particles in the plasma cloud interact with each other to form body forces. The ionized air, in the presence of the electric field, results in a body force vector that acts on the ambient (neutrally charged) air. The mobility and hence temperature and density of the particles are related to the Debye length. The Debye length and body force are also directly correlated.

We will start the derivation by considering the one-dimensional equation of motion for plasma gas Davidson (2001):

$$mn\left[\frac{\partial \mathbf{u}_p}{\partial t} + (\mathbf{u}_p \cdot \nabla) \mathbf{u}_p\right] = qn\mathbf{E} - \frac{\partial p_p}{\partial t} \quad (23)$$

where m refers to the mass of the ion particle (Kg), n refers to the number of particles in the plasma gas, \mathbf{u}_p is the plasma velocity (m/s), q is the charge of the particle (C) and p_p is the pressure of the plasma gas (Pa) and s denotes the spatial coordinate.

Ignoring the diffusion process and assuming steady state, the velocity gradients can be ignored. For an isothermal gas:

$$\frac{\partial p_p}{\partial t} = k_b T \frac{\partial n}{\partial s} \quad (24)$$

where k_b is the Boltzmann's constant ($1.3806503 \times 10^{-23} \text{ m}^2\text{kg/s}^2\text{K}$) and T is the temperature (K). Combining (23) and (24) gives:

$$qn\mathbf{E} = k_b T \frac{\partial n}{\partial s} \quad (25)$$

For the plasma under consideration, the ions lose only one electron and have the charge $q = -e$, where e is the charge of the electron (C). Applying $\mathbf{E} = -\partial\Phi/\partial s$, we obtain:

$$e \frac{\partial \Phi}{\partial s} = \frac{k_b T}{n} \frac{\partial n}{\partial s} \quad (26)$$

The solution for equation (26) is the Boltzmann relation:

$$n = n_0 \exp \frac{e\Phi}{k_b T} \quad (27)$$

where n_0 is the number of molecules that are separated into ions and electrons by the electric field, which is the so called background plasma density.

The charge density is the amount of electric charge in a volume and can be defined as the difference between the net positive charge produced by the ions and the net negative charge by the electrons. They can be related to the local electric potential, Φ , by the Boltzmann relation from equation (27). For a quasi-steady state with a time scale long enough for the charges to redistribute themselves, we obtain:

$$\rho_c = e(n_i - n_e) \approx -en_0 \left(\frac{e\Phi}{k_b T_i} + \frac{e\Phi}{k_b T_e} \right)$$

(28)

where T_i and T_e are the ion and electron temperature respectively (K).

Rewriting (28) leads to the electro-static equation:

$$\frac{\rho_c}{\epsilon_0} = -\frac{\Phi}{\lambda_D^2} \quad (29)$$

where λ_D is the Debye length (m) which is the characteristic length for electrostatic shielding in plasma. It is defined as:

$$\lambda_D = \left[\frac{e^2 n_0}{\epsilon_0} \left(\frac{1}{k_b T_i} + \frac{1}{k_b T_e} \right) \right]^{-1/2} \quad (30)$$

The SDBD is a form of laboratory gas discharge plasma, which has a Debye length in the order of 10^{-4} m according to Blandford et al. (2004) and Roth (1995). The Debye length is related to the physical properties of plasma. In Blandford et al. (2004), for a gas discharge operating at atmospheric pressure, a plasma density should form at a value of about 10^{15} to 10^{16} m⁻³. This corresponds to a Debye length value of approximately 0.17 mm was used initially in our study.

C. DIMENSIONALISED FORM

The S-H model is based from the Debye-Huckel approximation, where the electrical potential ϕ from the dielectric surface (double layer) has negligible effects on the simulation domain at low Debye lengths. The splitting of the electric potential results in the independence of the surface charge from the electrical field, as formulated in the model. To compute the Lorentz body force in Equation (21) we need the values of ρ_c and \mathbf{E} . These two values are obtained by decoupling the total electric potential term Φ into two parts:

$$\Phi = \phi + \varphi \quad (31)$$

where ϕ is the potential due to the external electric field and φ is the potential due to the charge density at the surface. Now we can proceed with a simplification of (21).

Since the Debye length λ_D is small and the charge on the dielectric surface is not large, the distribution of charged species in the domain is governed by the potential caused by the electric charge on the dielectric surface and is unaffected by the external electric field. This observation is made from the Debye-Huckel approximation, which relates the distribution of charge with surface potential of the wall. Its formulation can be traced in Henry (1931) and Saville (1977). An implementation into numerical modelling of electroosmotic flows is done by Patankar et al. (1998).

In COMSOL (2008), ρ_c is determined by φ , while the electric field, \mathbf{E} is governed by the potential ϕ . Therefore, we can write the Lorentz body force as:

$$\mathbf{F}_b = \rho_c (-\nabla \phi) \quad (32)$$

Note that this is different from Equation (21). The decoupling of the total electric potential enables us to rewrite equation (22) as two separate equations. The partial differential equation for the potential due to the electric field generated by the applied voltage is:

$$\nabla \cdot (\epsilon_r \nabla \phi) = 0 \quad (33)$$

The partial differential equation for the potential due to the net charge density is:

$$\nabla \cdot (\epsilon_r \nabla \varphi) = \rho_c / \epsilon_0$$

(34)

Furthermore, equation (29) yields:

$$\frac{\rho_c}{\varepsilon_0} = -\frac{\Phi}{\lambda_D^2} = \frac{\phi + \varphi}{\lambda_D^2} \rightarrow \varphi = \phi - \frac{\rho_c \lambda_D^2}{\varepsilon_0} \quad (35)$$

Substituting φ into equation (34) gives:

$$\nabla(\varepsilon_r \nabla(\phi - \frac{\rho_c \lambda_D^2}{\varepsilon_0})) = \frac{\rho_c}{\varepsilon_0} \quad (36)$$

which expanded yields:

$$\nabla(\varepsilon_r \nabla \phi) + \nabla(\varepsilon_r \nabla(\phi - \frac{\rho_c \lambda_D^2}{\varepsilon_0})) = \frac{\rho_c}{\varepsilon_0} \quad (37)$$

The first term in equation (37) is zero and we can rewrite the equation as:

$$\nabla(\varepsilon_r \nabla \rho_c) = \frac{\rho_c}{\lambda_D^2} \quad (38)$$

Once equations (33) and (38) are solved, the body force vector can be inserted into the Navier-Stokes computations as equation (32).

D. NON-DIMENSIONALISED FORM

Equations (33) and (38) can be solved initially before the Navier-Stokes equation as these equations do not contain a time derivative term. This is done by writing the terms into a non-dimensionalised form. The variables ϕ and ρ_c are non-dimensionalised to their values at the upper and lower electrodes respectively. The term ϕ_o is set as a boundary condition and refers to the applied AC voltage at upper electrode:

$$\phi_o(\tau) = \phi_{max} \times f(\tau) \quad (39)$$

where ϕ_{max} (V) refers to the maximum amplitude of the AC voltage supplied.

The term $\rho_{c,o}$ is set as a boundary condition at the lower electrode as:

$$\rho_c(\tau) = \rho_{c,max} \times f(\tau) \quad (40)$$

where $\rho_{c,max}$ (C/m³) refers to the maximum charge density of the AC voltage supplied.

The function $f(\tau)$ for the AC voltage source is:

$$f(\tau) = \sin(2\pi\tau) \quad (41)$$

where τ refers to a nondimensionalised time quantity.

We introduce the quantity by relating it to the frequency ω as:

$$\tau = \omega t$$

(42)

where ω (Hz) refers to the frequency of the AC voltage supply and is equal to 4.5 kHz in experiments (Jacob et al. (2005); Santhanakrishnan et al. (2009)). We also relate the frequency to the characteristic time, t_c as:

$$\omega = \frac{1}{t_c} \quad (43)$$

where $t_c = 2.22 \times 10^{-4}$ s. Note that this characteristic time is the time taken to complete one sinusoidal cycle and has the same order of 10^{-4} s as used in Enloe et al. (2004b). We solve the nondimensionalised time quantity, τ , from a value of 0 to 1. A time step of 0.01 is chosen to adequately observe the evolution of the induced fluid from the electrodes interface to the vortex formation at the right side of the domain.

The resulting non-dimensionalised quantities are:

$$\phi^* = \phi / \phi_0(\tau) \quad (44)$$

$$\rho_c^* = \rho_c / \rho_{c,0}(\tau) \quad (45)$$

$$F_b^* = F_b / \rho_{c,max} \times \phi_{max} \quad (46)$$

Therefore equation (33) becomes:

$$\nabla \cdot (\epsilon_r \nabla \phi^*) = 0 \quad (47)$$

And equation (38):

$$\nabla \cdot (\epsilon_r \nabla \rho_c^*) = \rho_c^* / \lambda_D^2 \quad (48)$$

The boundary condition for the upper electrode for ϕ^* is set to unity so that once ϕ^* is determined, the dimensional value ϕ can be obtained at any given time by multiplying the distribution with the corresponding value $\phi(\tau)$ given by equation (39). Similarly, the boundary condition for dielectric surface above the lower electrode for ρ_c^* is set to unity. This allows the dimensional value ρ_c to be obtained by multiplying the non-dimensionalised distribution ρ_c^* with the corresponding value $\rho_{c,0}(t)$ given in equation(45).

The characteristic λ_D value used for laboratory gas discharges is approximately 1.7×10^{-4} m, as shown in Roth (1995) and Thorne (2008). The maximum charged density, $\rho_{c,max}$, is set to 0.0075 C/m^3 as used in a previous simulation by Suzen et al. (2007). Later we will show that these two values govern the degree in which the body force will interact with the neutral fluid, and hence ‘tuning’ the values is required for a more accurate simulation of the plasma actuator. The maximum amplitude of the AC voltage supplied, ϕ_{max} , is set as 5 kV.

The value 0.0075 C/m^3 was used in Suzen et al. (2007), based on calibrations with flow patterns and maximum induced velocity. This is the value calibrated on a single case. The value is not universal and can be altered to affect flow patterns and induced velocity. The goal of the paper is to investigate these effects. We do not seek a universal value here, but we want to show what effect one can expect from varying the value.

Equations (47) and (48) are the governing equations used to model the non-dimensionalised body force in COMSOL. This means that they can be solved separately from the Navier Stokes equations. The dimensionalised body force can be obtained in (46) and can be inserted into the Navier-Stokes computations as equation (32).

Finally, the governing equations (47), (48) and (13), and the boundary equations are shown together with the geometries in Figure 3, Figure 4 and Figure 5 respectively. The terms GE and BC refer to governing equation and boundary conditions respectively.

4. COMPUTER RESOURCES

The system used for COMSOL simulations is a Dell workstation model E5520 with dual quad-core processors running at 2.26GHz. The workstation has 24GB of installed memory (RAM) and used Windows 7 Professional as its operating system.

The simulations are solved using the finite element computational package, COMSOL Multiphysics™ 3.5a COMSOL (2008). The ruling application mode for the investigation was the Incompressible Navier- Stokes application. The solver settings are based on the ruling application model. The application mode also uses Lagrange p2-p1 elements to stabilize the pressure. Thus 2nd-order Lagrange elements model the velocity components while linear elements model the pressure.

The step converges if the following condition is met:

$$\left(\frac{1}{N} \sum (\frac{|E_i|}{A_i + R|U_i|})^2 \right)^{1/2} < 1 \quad (49)$$

where A_i is the absolute tolerance for degree of freedom i , R is the relative tolerance, and N is the number of degrees of freedom. The estimated local error is typically of the same order of magnitude as the true global error COMSOL (2008). The method used to solve the time-dependent problem was the backward differentiation formula (BDF). BDF is a robust method that is commonly used for a wide range of problems. The algorithm for this method can be further read in Hindmarsh et al. Hindmarsh et al. (2005).

Since the electric potential (47) and surface charge equations (48) are decoupled from the Navier-Stokes equation (13), a segregated solver approach can be used. In this approach, the variables in the first two equations (ϕ^* and ρ_c^*) are grouped together, while the variables in the N-S equations (u, v, p) form the other group. The error analysis for the parametric $\rho_{c,max}$ and λ_D studies are shown in Figure 6 Both figures show that that the two groups satisfy the absolute error of 10^{-6} before the next stipulated step.

The Navier-Stokes equation in COMSOL uses three artificial diffusion techniques: the Galerkin Least-Squares (GLS), crosswind and isotropic diffusion COMSOL (2008). These techniques add terms to the transport equation to stabilize the solution. The GLS technique is a form of streamline diffusion that adds higher-ordered superviscosity terms and provides extra stability. Crosswind diffusion addresses the sharp gradients that may occur during the simulation. The terms add diffusion orthogonal to the streamline direction and are mostly consistent and do not alter the equation. The isotropic diffusion technique introduces an artificial diffusion coefficient to the Peclet number so that it never exceeds unity.

The mesh density is within the stipulated Debye length order and the resolution check is described in a previous paper by Ibrahim et al. (2010). The maximum velocities are compared with previous numerical works (Suzen et al. (2005); Suzen et al. (2006); Reasor Jr et al. (2007); Suzen et al. (2007)) and experimental works (Jacob et al. (2005); Santhanakrishnan et al. (2009)). The electrical potential results are compared with previous computational models, while velocity vectors and streamline plots are compared with experiments. It should be noted that the experimental data is also somewhat preliminary and it is used here only to demonstrate the feasibility of the modelling approach of the plasma actuator. There is no external flow - all flows are generated by the action of the plasma actuator.

5. RESULTS

The electrical potential results are compared with previous computational models (Suzen et al. (2005); Suzen et al. (2006); Reasor Jr et al. (2007); Suzen et al. (2007)), while velocity vectors and streamline plots are compared with experiments (Jacob et al. (2005); Santhanakrishnan et al. (2009)). The comparisons of the Suzen-Huang model with experimental results demonstrate the feasibility of the modelling approach of the plasma actuator. However, the results of the simulations overpredict the maximum velocity observed in experiments. Two scalar quantities, the Debye length (λ_D) and maximum charge density ($\rho_{c,max}$), are altered to better match the velocity profiles obtained in the experiments.

A. VALIDATIONS

Studies have shown that plasma light intensity can be taken as a ‘surrogate’ to charged plasma density. Scanning the photomultiplier tube (PMT) over the surface and taking data synchronized with the AC voltage has shown that a spatial and temporal map of the extent of the plasma in the chordwise direction can be formed Enloe et al. (2004b); Enloe et al. (2004c).

This map corresponds to the non-dimensionalised charge density ρ_c^* distribution at the top of the encapsulated electrode which is shown in Figure 7. The figure shows that the discharge ignites near the edge of the exposed electrode and that the extent of the plasma in the chordwise direction increases in time until the discharge quenches, when the AC voltage reaches a peak value.

Figure 8 shows the distribution of electric field strength (E) on top of the encapsulated electrode. It shows that the highest electric field strength is located at the edge of the exposed electrode. The decrease in strength across the gap of the two electrodes can also be seen when the plot is ranged from 10^5 to 10^7 V/m. The uncoloured area next to the exposed electrode represents the electric strength magnitude of above 10^7 V/m.

The flux of the electric field is shown in Figure 9. Near the gap, the vectors point from the upper to lower electrodes. This general direction of the electric field vectors remains downstream towards the lower electrode. The magnitude of the electric field decreases away from the gap. This in turn affects the distribution of the body force, which resembles that of an exponential function as noted by several investigations (Enloe et al. (2004a); Enloe et al. (2004b); Enloe et al. (2006)).

From the ρ_c^* and E plots, we can expect the strength of the body force to reach a maximum at the top surface of the leading edge of the lower electrode. The non-dimensionalised body force distribution obtained from equation (46) is shown in Figure 10. The distribution of the body force initiates from the end of the upper electrode and increases at the gap between the two electrodes. As correctly anticipated, it reaches a maximum at the top surface of the leading edge of the lower electrode and gradually decreases towards the extent of the electrode. The distribution is governed by the electric field strength and charge density distribution as described by equation (45). It only reaches its maximum at the surface of the upper left corner of the lower electrode. (See Figure 7)

Figure 10 also shows the resultant induced velocity U , from the plasma actuation from the present simulation in COMSOL. Induced velocity is defined as the resultant velocities of the u - and v -vectors:

$$U = \sqrt{u^2 + v^2} \quad (50)$$

Figure 11 shows the non-dimensionalised electrical potential ϕ^* comparison with simulations done in GHOST in Suzen et al. (2007) and COMSOL. The comparisons show good general agreement. The contours are denser near the gap of the electrodes and spreads out evenly further away from the electrodes. The curvatures of the streamline become more pronounced at the surface of the lower electrode, indicating that the fluid is sucked in towards the area before being pushed downstream of the lower electrode.

Simulation results are compared with experimental data by Jacob et al. (2005) and Santhanakrishnan et al. (2009). Two figures are compared: the streamline and velocity profile plots. The figures represent the induced velocities in a quiescent environment. The experimental and computational streamline plots are shown in Figure 12. Experimental results indicate that the flow is drawn into the surface region above the embedded electrode by the plasma induced body force. This resulted in a jet issuing to the right of the actuator with a maximum velocity of approximately 1 m/s. The experimental (left) plots show that the lines are pulled in from all directions and produce a virtual outlet at the bottom right side of the diagram. The curvature of the streamlines towards the outlet is most pronounced at the middle portion of the encapsulated electrode (here positioned at the 0.025-0.026 m tick). At the left side of the lower electrode (from the 0.02-0.025 m tick), there is a suction of fluid that is present in the experiment that was not adequately captured by simulations conducted by neither GHOST in Suzen et al. (2007) nor COMSOL. The velocity profiles at the region will highlight these differences and are utilized to propose several modelling amendments. At the right side of the lower electrode (from the 0.025-0.03 m tick), the streamlines follow the profile towards the outlet at the bottom right side.

The computational result (right plot in Figure 12) shows a similar streamline profile compared to the experiments. The arrowheads for each streamline are not shown, but the general directions of the streamlines are as follows: suction towards the 0.02 – 0.025 m tick from almost all the boundaries of the domain except for the outlet section at the bottom right portion. The boundary layer thickness is also slightly thinner compared to the experimental results.

Figure 13 shows the u -velocity profiles plot of eight stations taken downstream and upstream of the plasma actuator interface. The profiles obtained from experiment by Santhanakrishnan et al. (2009) (left) show that there is a gradual increase of u -velocity from the interface to the furthest station at 1.6 cm downstream. The maximum velocity reached is approximately 1 m/s, while the maximum velocity of the simulation is about 1.88m/s. This maximum velocity obtained in the simulation lie at 0.001 m downstream from the interface and is not shown in Figure 13. The velocity obtained at 0.004 m downstream from the interface from our simulation was 1m/s, which corresponded to the maximum velocity obtained from the experiments. The peak velocity decreases for stations downstream of the lower electrode. The thickness of the velocity profiles in the experimental results shows that more fluid is being pushed by the body force than that is captured by our simulation.

In Figure 14, the normal velocity component (v) from experiments and simulations is shown. The experimental results suggest that the location of the largest v -velocity is at the end of the exposed electrode. The value obtained from experiments is 0.43 m/s which are slightly larger than the COMSOL simulation value of 0.38 m/s. The lower maximum v -velocity is also consistent with the thinner boundary layer what was observed in Figure 12.

B. EFFECTS OF INCREASING DEBYE LENGTH

From the comparisons with experimental data, it can be deduced that for an accurate depiction of quiescent flow environment, the location and vector characteristics of the body force has to be corrected. The force acting on the fluid domain should be present at a higher position than the exposed electrode. Also its intensity should increase and the position of the maximum should be positioned near the end of the top surface of the encapsulated electrode, so that a maximum velocity is achieved at a similar position.

It is hypothesized that the simulation would be better matched with experimental data by varying the scalar parameters that were used in the modelling. The two scalar parameters that can be altered are the Debye length λ_D and the maximum charge density $\rho_{c,max}$. Their effects on the charge density propagation and body force distribution are discussed next. Changes to the Debye length and maximum charge density do not affect the electric field distribution, as the electric field is governed by equation (34).

I. CHARGE DENSITY PROPAGATION

In this analysis, $\rho_{c,max}$ is kept at the prescribed value of 0.00075 C/m³. The Debye length is parametrically increased from a value of 10⁻⁵ m to 10⁻³ m with a linear step value of 1.1 x 10⁻⁴ m. In equation (38), the Debye length is a scalar variable in the source term of the equation that affects the degree of charge density propagation. As this length increases, the source term in equation (38) becomes smaller. This results in the charge density developing into the regions above the exposed electrode height.

Figure 15 shows the changes in the non-dimensional charge density distribution when the Debye lengths are at the lower and upper limits of the parametric study. The non-dimensionalised charge density grows from a negligible state when $\lambda_D = 10^{-5}$ m (not shown) to 0.002 m above the exposed electrode at $\lambda_D = 1.2 \times 10^{-4}$ m. The charge density value increased about 260% when λ_D changed from 10⁻⁵ m to 1.2 x 10⁻⁴ m. However, the charge density value only increased about 0.42% when λ_D changed from 8.9 x 10⁻⁴ m to 0.001 m. This shows that the growth increases at a higher rate at lower incremental Debye length values (Shown in Figure 17). The propagation grows to a maximum height of about 0.003.

In Figure 16, a cross sectional plot of the vertical distance versus the non-dimensional charge density is shown from the top left corner of the encapsulated electrode (when $x = 0.0205$ m shown in Figure 10) for all parametric values. Two observations can be made. Firstly, the maximum value of the non-dimensional charge density increases in a non-linear manner with increasing Debye length. This can be seen from the values at the zero value of the y -coordinate. For a Debye length of 10⁻⁵ m, the non-dimensional charge density value corresponds to 0.18. For the remaining Debye lengths which were investigated, the non-dimensionalised values had a range from 0.66 to 0.85. Secondly, the height of the non-dimensionalised charge density increases linearly with increasing Debye length. For example, at the

non-dimensional charge density value corresponding to 0.1, the spaces of the functions between each increasing Debye length are of equal magnitude (see spaces between the black lines in Figure 16).

The non-linear relationship between ρ_c^* and λ_D at $y = 0$ is shown in Figure 17. The value of ρ_c^* increases from 0.18 to 0.66 at the first increment of λ_D . It reaches a maximum value of 0.82. The non-linear increments of the maximum charge density and the linear increments of space propagations distance are a result from the fact that the scalar Debye length is only present in the governing equation in the air domain from equation (33). At the Kapton, the source term is zero. Also, the non-linear increments of the maximum charge density as well as the linear increments of space propagations can be explained by the difference in the permittivity of Kapton and air. Since the boundary condition is imposed at the lower electrode, the value of the maximum non-dimensional charge density is governed by the permittivity of Kapton, which as a value of 2.7. Once the air domain is reached, the propagation increases linearly because of the unity value used as permittivity in air.

II. BODY FORCE PROPAGATION

The resulting non-dimensionalised body force figures from the parametric increments of the Debye length are shown in Figure 18. The figure obtained correlates with the growth of the charge densities as seen from Figure 15. A small region of body force exist at the top surface of the lower electrode when $\lambda_D = 10^{-5}$ m (not shown). It substantially increases to about 946 when $\lambda_D = 1.2 \times 10^{-4}$ m. The increment becomes gradual from $\lambda_D = 2.3 \times 10^{-4}$ m to $\lambda_D = 0.001$ m as shown in Figure 18; a character which corresponds to the charge density propagation.

The body forces initiates at the end of the exposed electrode and grows to a maximum at the leading edge of the lower electrode. Then the intensity of the force gradually decreases towards the end lower electrode. Figure 19 shows a cross sectional plot of the vertical distance versus the non-dimensional body force. The results are obtained from the top left corner of the encapsulated electrode (when $x = 0.0205$ m in the simulation domain in Figure 10) for all parametric values. The results are similar to that seen in the parametric study in Figure 18 of the non-dimensional charge densities in that they show a linear relationship with the increasing Debye length.

The non-linear relationship between ρ_c^* and λ_D at $y = 0$ is shown in Figure 20. The value of F_b^* increases from 220 to 910 at the first increment of λ_D . It reaches a maximum value of 1200.

III. INDUCED VELOCITY

The effects on the induced velocity are more substantial with increasing values of Debye length. Figure 21 shows the effects of increasing Debye length on the induced velocity near the electrodes. When $\lambda_D = 1.2 \times 10^{-4}$ m, an induced velocity of about 1.48 m/s can be seen. When it is increased to 0.001m, more fluid is entrained and the magnitude increased to 3.55 m/s. There is also small induced fluid motion towards the exposed electrode. This signifies that a small body force is acting towards that direction.

The induced force does not impose a strong enough push in the horizontal direction for the jet to develop because of the small Debye length results in a low charge density presence. The force in the x-direction increases in strength and the point corresponding to the maximum velocity moves to the right when $\lambda_D = 0.00012$ m. The trend continues as λ_D increases. Another observation that can be made is the shift in the location of the point of maximum velocity region towards the right. At higher values of the Debye length, the body force is exerted on a larger area of the fluid domain, leading to entrainment. The additional momentum pushes the maximum velocity towards the right.

C. EFFECTS OF INCREASING MAXIMUM CHARGE DENSITY

Next, a parametric analysis is conducted on the maximum charge density value, denoted as $\rho_{c,max}$ in the simulations. The Debye length is kept at the experimental value of 0.17 mm. The range for the maximum charge densities is from 0.00001 C/m^3 to 0.001 C/m^3 , similar to that studied in the parametric analysis of the Debye length. The previous maximum charge density value used was 0.00075 C/m^3 . The emphasis of the study in this section will be the effect on the induced velocity since the effect on the body force varies linearly with the maximum charge density, as seen from equation (32).

I. INDUCED VELOCITY

The effect on the induced velocity near the electrodes shows varying profiles in Figure 22. The location of the point of maximum induced velocity, denoted by the black point in the figures, remains static throughout the parametric increments unlike the shift observed when Debye length is increased (shown in Figure 21). Furthermore, the increase in magnitudes of the induced velocity does not increase as much compared to the previous Debye length study in Figure 21. The Debye length increment had recorded a maximum induced velocity of 3.5 m/s, while the maximum velocity seen in Figure 22 is 0.46 m/s.

D. THE RESULTANT VELOCITY PROFILES IN QUIESCENT ENVIRONMENT

Experimental results in Figure 13 and Figure 14 suggest that the induced jet propagates further down the encapsulated electrode. The induced velocity also reaches a maximum after the encapsulated electrode. This implies that the charge density has to be more expansive than that modelled initially. The size of the charge density has to be modelled larger. However, the strength of the charge density has to be limited so that the magnitude of the induced velocity would not be too excessive.

The main conclusion that can be drawn from the previous analysis is that although both the Debye length and maximum charge density parameters has an effect on the size and strength of the body force induced velocity, the Debye length has a more substantial effect compared to the maximum charge density. Figure 21 showed the effects of increasing the Debye length with a constant $\rho_{c,max}$ value of 0.0075 C/m^3 . The induced velocity reached a maximum value of 3.5 m/s. Also, although the location of this maximum point moves downstream of the encapsulated electrode with increasing Debye length, at Debye length equal to 0.001m, the location of the maximum is still within the encapsulated electrode. It is clear that a higher Debye length (compared to the values used in the parametric analysis) is required to push the maximum point away from encapsulated electrode. A lower $\rho_{c,max}$ value is also needed in order to keep the value of the induced velocity limited.

Based from these observations, the model is then simulated with the Debye length and maximum charge density values of 0.005 m and 0.0005 C/m^3 respectively. From our understanding, these conditions will result in a highly dense gas discharge. The maximum induced velocity with these values of the parameters is 1m/s. The resultant u and v-velocity profiles of the eight stations are shown in Figure 23. The *u*-velocity profiles for this simulation show better agreement in terms of downstream strength and jet thickness, but are still not as strong as the observed experimental flow at the most downstream location of 1.6 cm from the exposed electrode interface. At the location of 1.6 cm downstream from the interface (as denoted by the brown line), the profile is very close to the velocity profile at location 1.2cm downstream. These velocity profiles also over-predict the contribution of the horizontal component of the body force near the electrode interface. The maximum negative *v*-velocity is still observed at the interface, but has smaller magnitude than that observed in the experiment for the interface location. At the locations at 1.2 cm and 1.6 cm downstream the *v*-velocity magnitude shows good agreement with the experiment and hence demonstrates that the upward component body force in the computations is similar to that observed experimentally.

6. CONCLUSION

Plasma actuator models could be simulated with less computing resources when utilizing the S-H model, compared to the charge transport models. This is because trajectories of the individual charge particles have to be initially calculated for the charge transport models. In addition, since the model is originally defined for a flow control study, detailed evolutionary aspects of the charge density term is not as important as determining the final induced velocities of the plasma actuator. However, one should observe that while simplifying the physical model from microscopic to macroscopic form has many benefits as described above, the main drawback is that the parameters in the model to some extent lose their physical meaning, and furthermore, calibration of the model might be needed for each application. This scenario is of course not unique, and can be found in many fields where the reduction of complicated physics leads to non-physical and recalibrated parameters, most notably in the area of turbulence modelling.

A parametric analysis is conducted on the scalar variables of the Suzen-Huang model. By varying scalar values of Debye length and maximum charge density, the effects of charge density, body force and induced velocity are examined. A linear variation was already deduced from the relationship between the magnitude of the non-dimensionalised body force and the maximum charge density. Simulations however indicate that the magnitude of the non-dimensionalised body force is nonlinearly related to the Debye length. The results show that the location and strength of the maximum induced velocity can be tuned to the experimental data by varying the scalar variables λ_D and $\rho_{c,max}$. However, the body force still has to be modelled more extensively above the encapsulated electrode because the discrepancies are due to the absence of a more prominent body force above the dielectric. The terms defining the Debye length can be included to further analyze the effects on the model. For example, the inclusion of a variable λ_D could result in more accurate horizontal and vertical components of the induced velocities.

REFERENCES

1. Blandford RD and Thorne K (2004). *Applications of Classical Physics*. California, USA, Caltech: p. 980.
2. Boeuf JP and Pitchford LC (2005). Electrohydrodynamic force and aerodynamic flow acceleration in surface dielectric barrier discharge. *Journal of Applied Physics* 97(10): 1-10.
3. COMSOL (2008). *COMSOL Multiphysics Modeling Guide*.
4. Corke TC, Post ML and Orlov DM (2008). Single Dielectric Barrier Discharge Plasma Enhanced Aerodynamics: Concepts, Optimization and Applications *Journal of Propulsion and Power* 24(5): 935-945.
5. Corke TC, Post ML and Orlov DM (2009). Single dielectric barrier discharge plasma enhanced aerodynamics: Physics, modeling and applications (Review Article). *Experimental Fluids*(46): 1-26.
6. Davidson PA (2001). *An Introduction to Magnetohydrodynamics*. Cambridge, Cambridge University Press.
7. Enloe CL, McLaughlin TE, Font GI and Baughn JW (2006). Parameterization of temporal structure in the single-dielectric-barrier aerodynamic plasma actuator. *AIAA Journal* 44(6): 1127-1136.
8. Enloe CL, McLaughlin TE, Vandyken RD and Fischer JC (2004a). Plasma structure in the aerodynamic plasma actuator. *AIAA-2004-0844*.
9. Enloe CL, McLaughlin TE, VanDyken RD, Kachner KD, Jumper EJ and Corke TC (2004b). Mechanisms and Responses of a Single Dielectric Barrier Plasma Actuator: Geometric Effects. *AIAA Journal* 42(3): 595-604.
10. Enloe CL, McLaughlin TE, VanDyken RD, Kachner KD, Jumper EJ and Corke TC (2004c). Mechanisms and Responses of a Single Dielectric Barrier Plasma Actuator: Plasma Morphology. *AIAA Journal* 42(3): 589-594.
11. Henry DC (1931). The Cataphoresis of Suspended Particles. Part I. The Equation of Cataphoresis. *Proceedings of the Royal Society of London. Series A, Containing Papers of a Mathematical and Physical Character* 133(821): 106 - 129.
12. Hindmarsh AC, Brown PN, Grant KE, Lee SL, Serban R, Shumaker DE and Woodward CS (2005). SUNDIALS: Suite of nonlinear and differential/algebraic equation solvers. *ACM Transactions on Mathematical Software* 31(3): 363-396.
13. Ibrahim IH and Skote M (2010). Modeling the Plasma Actuator via the Splitting of the Electric Potential. *Icms2010: Proceedings of the Third International Conference on Modelling and Simulation, Vol 2 - Modelling and Simulation in Engineering*. Jiang Y and Chen X. Liverpool, World Acad Union-World Acad Press: 1-6.
14. Jacob JD, Karthik R, Anthony R and Rivir RB (2005). Control of Laminar and Turbulent Shear Flows Using Plasma Actuators. *4th International Symposium on Turbulence and Shear Flow Phenomena*, Williamsburg, VA.
15. Jayaraman B, Thakur S and Shyy W (2007). Modeling of fluid dynamics and heat transfer induced by dielectric barrier plasma actuator. *Journal of Heat Transfer* 129(4): 517-525.
16. Massines F, Rabehi A, Decomps P, Gadri RB, Seĭgur P and Mayoux C (1998). Experimental and theoretical study of a glow discharge at atmospheric pressure controlled by dielectric barrier. *Journal of Applied Physics* 83(6): 2950-2957.
17. Orlov DM (2006). *Modelling and Simulation Of Single Dielectric Barrier Discharge Plasma Actuators*. Aerospace and Mechanical Engineering. Notre Dame, Indiana, University of Notre Dame. Doctor of Philosophy: 189 pages.
18. Orlov DM, Apker T, He C, Othman H and Corke TC (2007). *Modeling and Experiment of Leading Edge Separation Using SDBD Plasma Actuators*. 45th AIAA Aerospace Sciences Meeting and Exhibit. AIAA. Reno, Nevada, AIAA 2007-0877: 1-18.
19. Orlov DM and Corke TC (2005). Numerical simulation of aerodynamic plasma actuator effects. *43rd AIAA Aerospace Sciences Meeting and Exhibit - Meeting Papers (also in AIAA 2005-1083)*.
20. Orlov DM, Corke TC and Patel MP (2006). Electric Circuit Model for the Aerodynamic Plasma Actuator. *AIAA Journal* 19: 14678-14687.
21. Patankar NA and Hu HH (1998). Numerical Simulation of Electroosmotic Flow. *Analytical Chemistry*(70): 1870-1881.

22. Reasor Jr DA, LeBeau Jr RP and Suzen YB (2007). Unstructured grid simulations of plasma actuator models. *Collection of Technical Papers - 37th AIAA Fluid Dynamics Conference AIAA 2007-3973*, Miami, Florida.
23. Roth JR (2001). Electrohydrodynamic (EHD) Flow Control. *Industrial Plasma Engineering Volume 2: Applications to Non-Thermal Plasma Processing*, Institute of Physics Publishing. 2: Applications to Non-Thermal Plasma Processing: 225-237.
24. Roth JR (1998). Electrohydrodynamically induced airflow in a one atmosphere uniform glow discharge surface plasma. *25th IEEE Int. Conf. Plasma Science*, USA.
25. Roth JR (1995). DC Electrical Glow Discharge in Gases. *Industrial Plasma Engineering Volume 1: Principles*, Institute of Physics Publishing 1: Principles: 284-351.
26. Roth JR, Sherman DM and Wilkinson SP (1998). Boundary layer flow control with a one atmosphere uniform glow discharge surface plasma. *36th Aerospace Sciences Meeting & Exhibit*, Reno, Nevada.
27. Rouffet J-B (2008). Plasma Actuator Influence on Air Flow. *COMSOL Conference 2008*, Hannover, COMSOL.
28. Roy S and Wang CC (2008). Plasma actuated heat transfer. *Applied Physics Letters* 92(23).
29. Santhanakrishnan A, Reasor Jr DA and LeBeau Jr RP (2009). Characterization of linear plasma synthetic jet actuators in an initially quiescent medium. *Physics of Fluids* 21(4).
30. Saville DA (1977). Electrokinetic effects with small particles. *Annual Review Of Fluid Mechanic* 9: 321–337.
31. Singh KP and Roy S (2005). Simulation of an asymmetric single dielectric barrier plasma actuator. *Journal of Applied Physics* 98(8): 1-7.
32. Suzen YB and Huang PG (2006). Simulations of flow separation control using plasma actuators. *44th AIAA Aerospace Sciences Meeting and Exhibit AIAA 2006-877*, Reno, Nevada.
33. Suzen YB, Huang PG and Ashpis DE (2007). *Numerical simulations of flow separation control in low-pressure turbines using plasma actuators*. 45th AIAA Aerospace Sciences Meeting, Toronto, Ontario Canada. 16: 11358-11365.
34. Suzen YB, Huang PG, Jacob JD and Ashpis DE (2005). *Numerical simulations of plasma based flow control applications*. 35th AIAA Fluid Dynamics Conference and Exhibit: 1-11.
35. Thorne K (2008). *Application Of Classical Physics - Chapter 19: The Particle Kinetics of Plasma*. California, Caltech: 33.

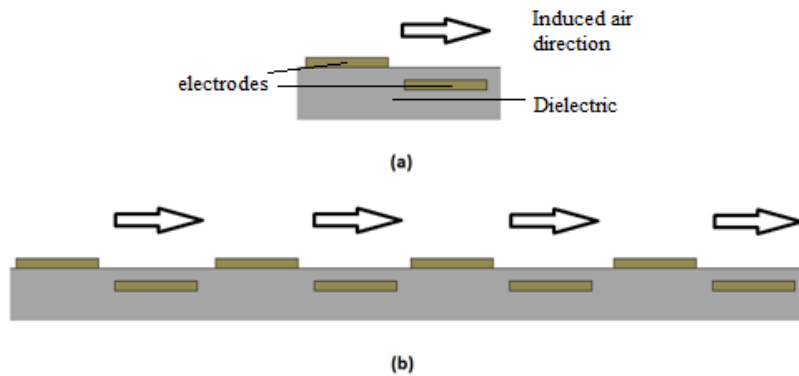


Figure 1: A single (a) and an array (b) of electrodes that induces fluid motion to the right. Figure adapted from Roth (2001).

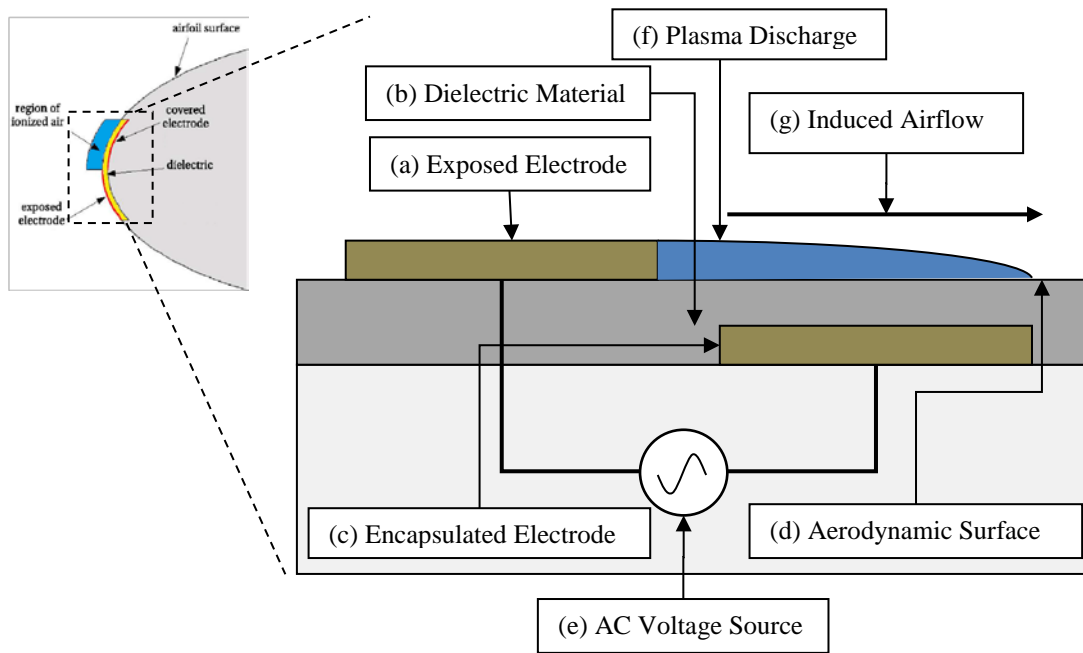


Figure 2: The plasma actuator in chord wise section by Orlov (2006). The blue region represents the plasma discharge.

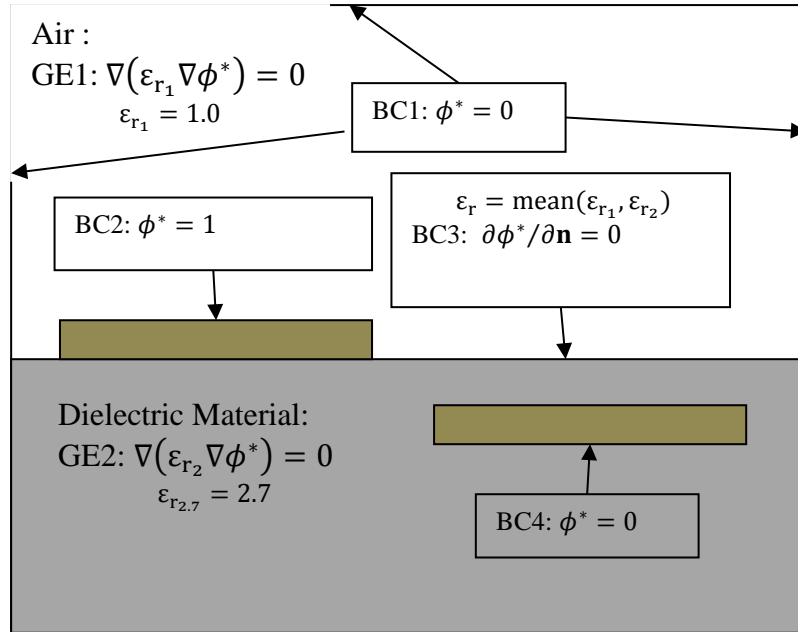


Figure 3: Subdomain and boundary conditions for Equation (33).

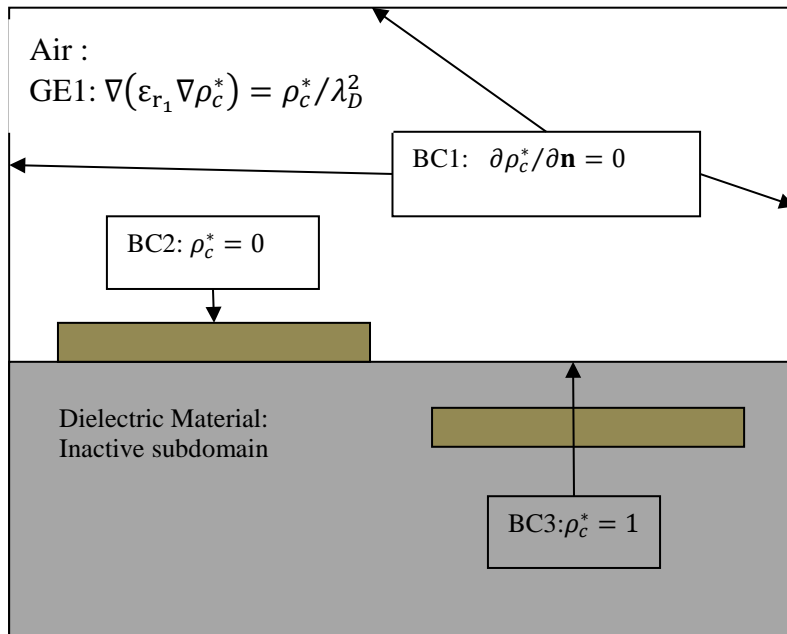


Figure 4: Subdomain and boundary conditions for Equation (38).

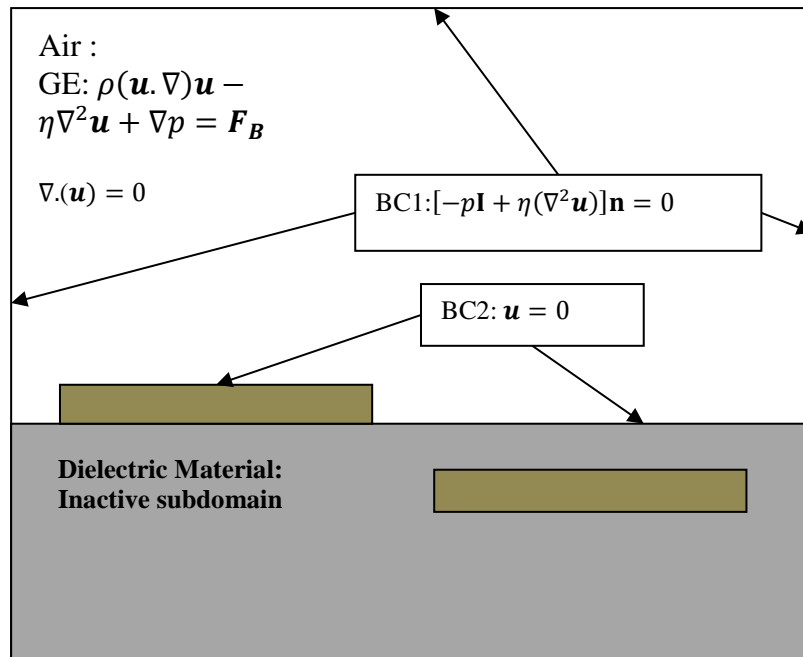


Figure 5: Subdomain and boundary conditions for Equation (13).

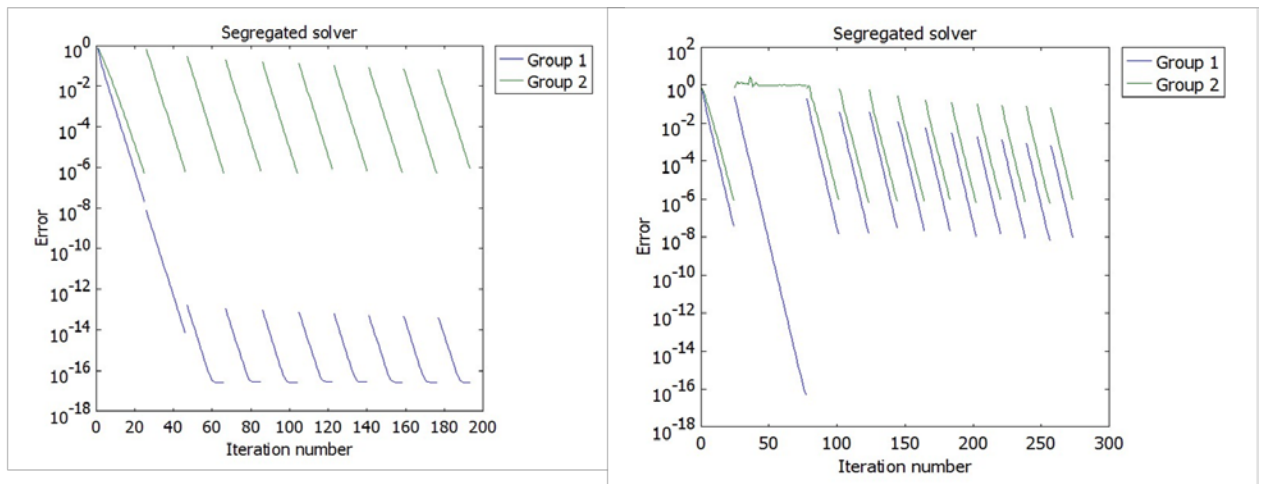


Figure 6 Convergence history for $\rho_{c,max}$ (left) and λ_D (right).

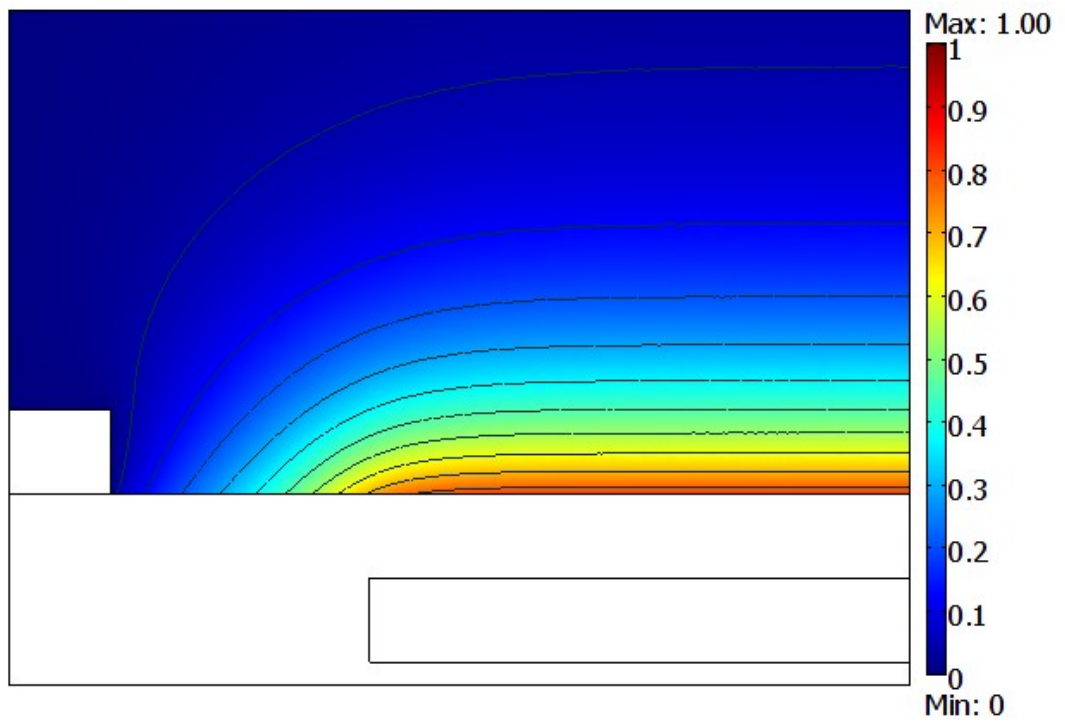


Figure 7: Non-dimensionalized charge density surface distribution on top of the encapsulated electrode.

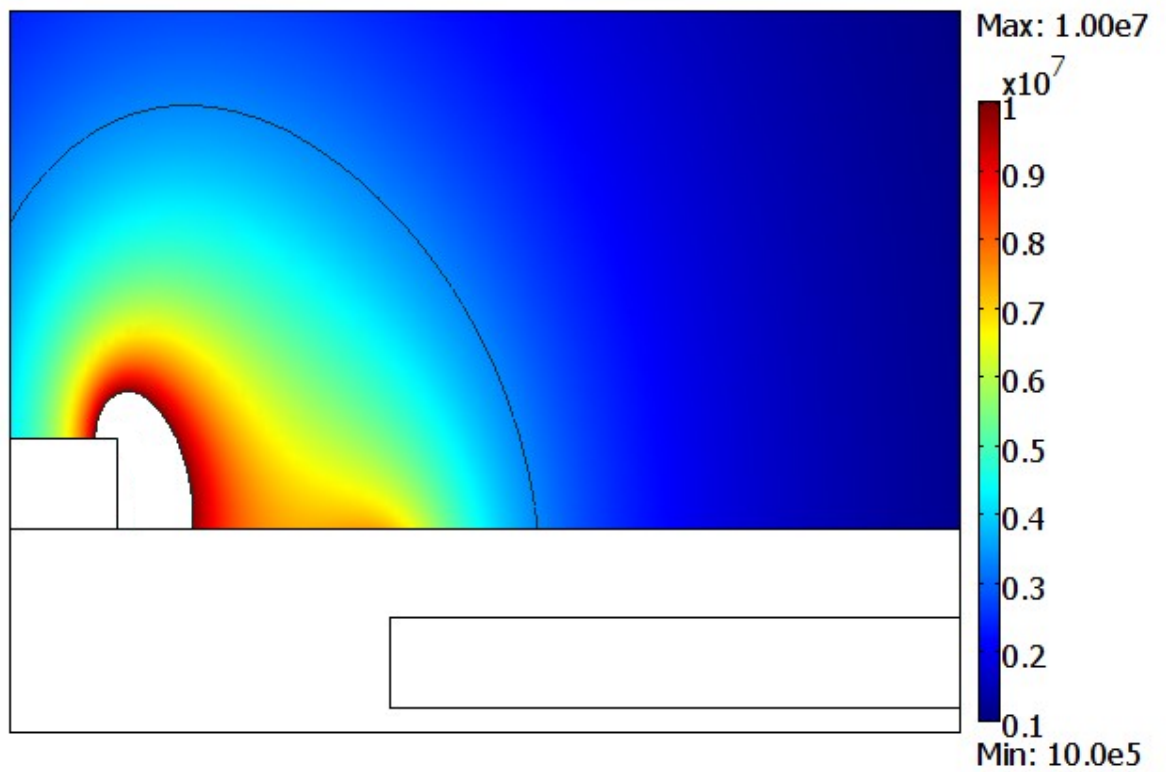


Figure 8: Electric field strength distribution (ranged from 10^5 to 10^7 V/m) on top of the encapsulated electrode.

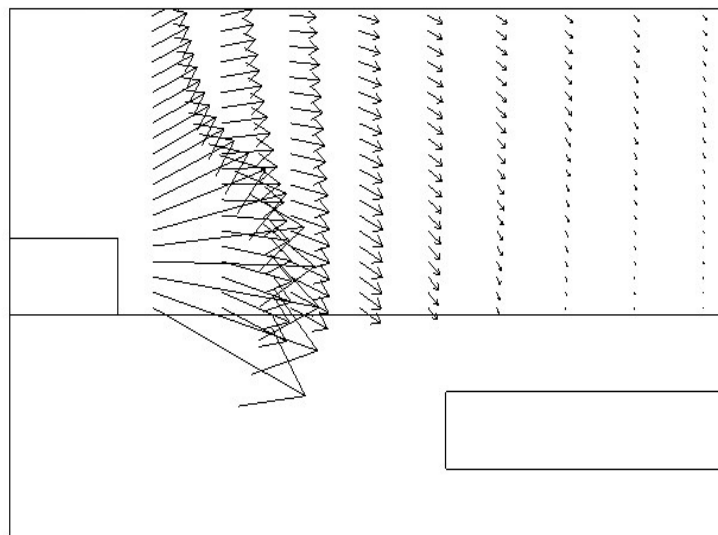


Figure 9: Electric flux vectors present on near the gap and at the top of the encapsulated electrode.

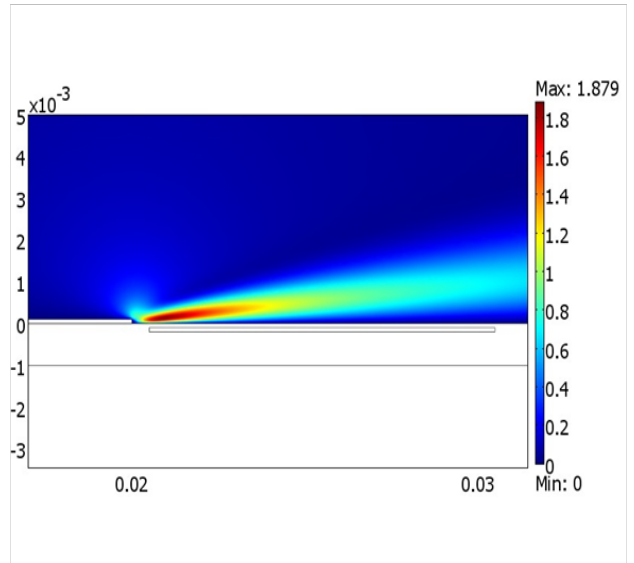
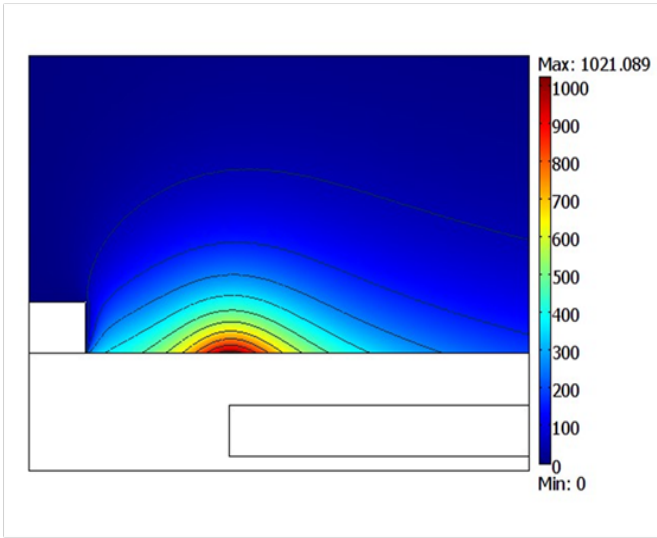


Figure 10: The non-dimensionalised body force surface plot (left) shows a maximum value near the surface of the upper left corner of the lower electrode. The resulting induced velocity (right) at the top surface of the encapsulated electrode.

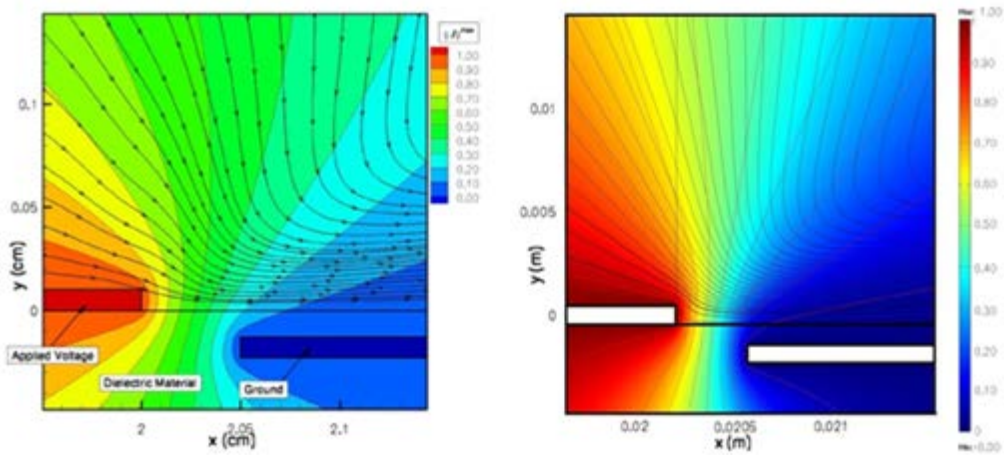


Figure 11: Comparison of the electric potential contours from simulations done in GHOST in Suzen et al. (2007) and COMSOL.

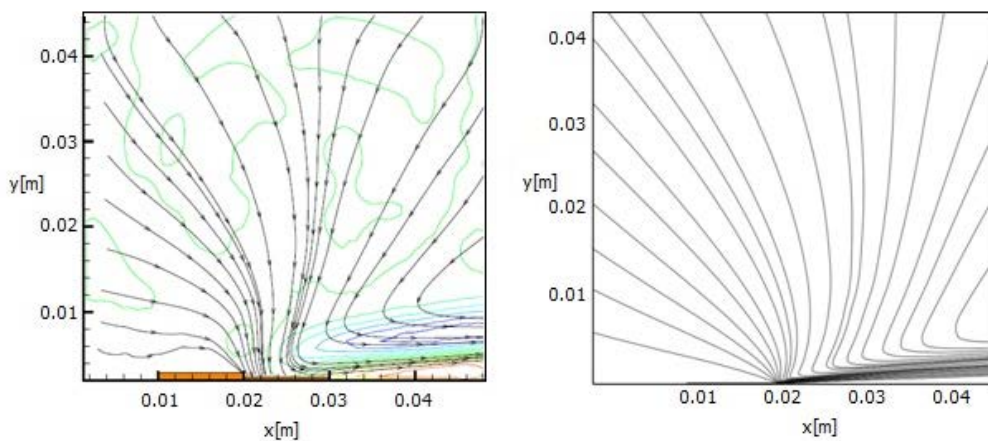


Figure 12: Quiescent flow streamline plots obtained from experiment Jacob et al. (2005) (left) and COMSOL (right).

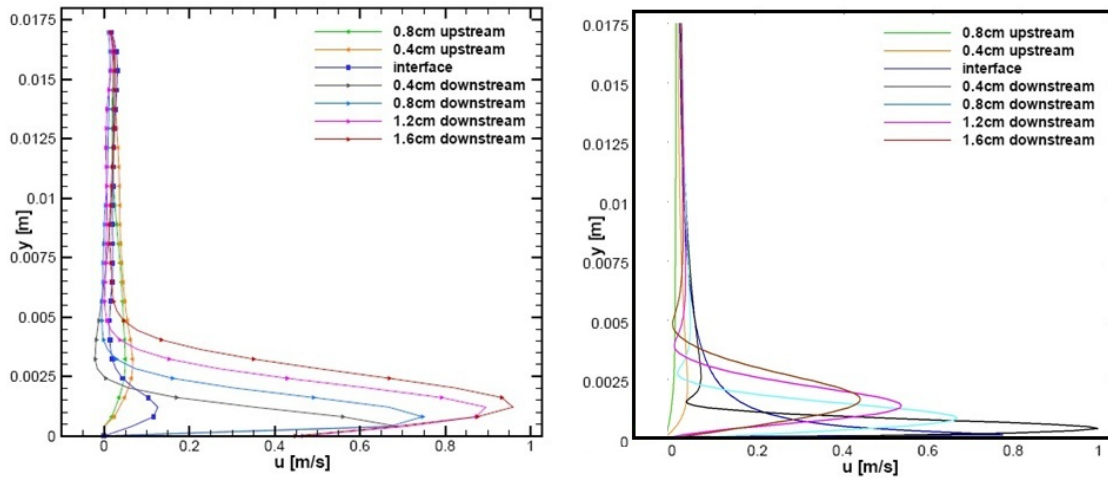


Figure 13: The u-velocity profiles of 8 stations taken from experimental by Santhanakrishnan et al. (2009) (left) and COMSOL (right) results.

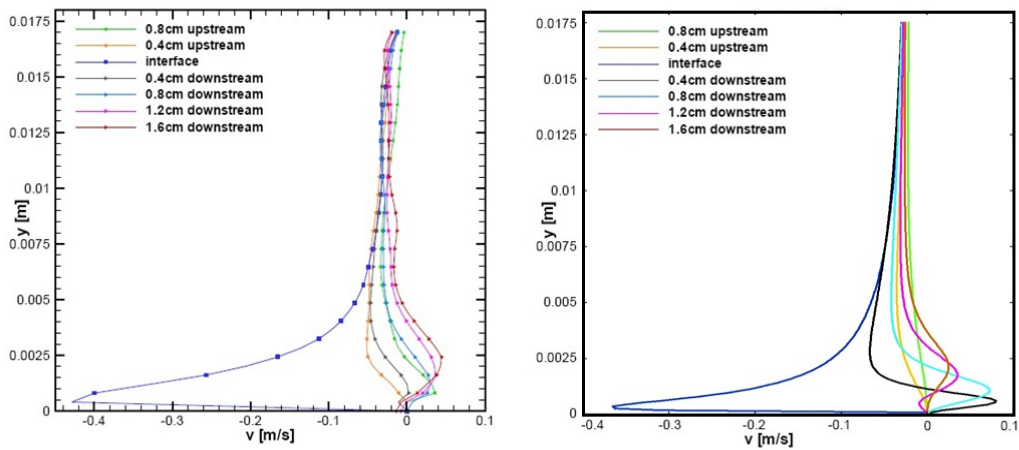


Figure 14: The v-velocity profiles of 8 stations taken from experimental by Santhanakrishnan et al. (2009) (left) and COMSOL (right) results.

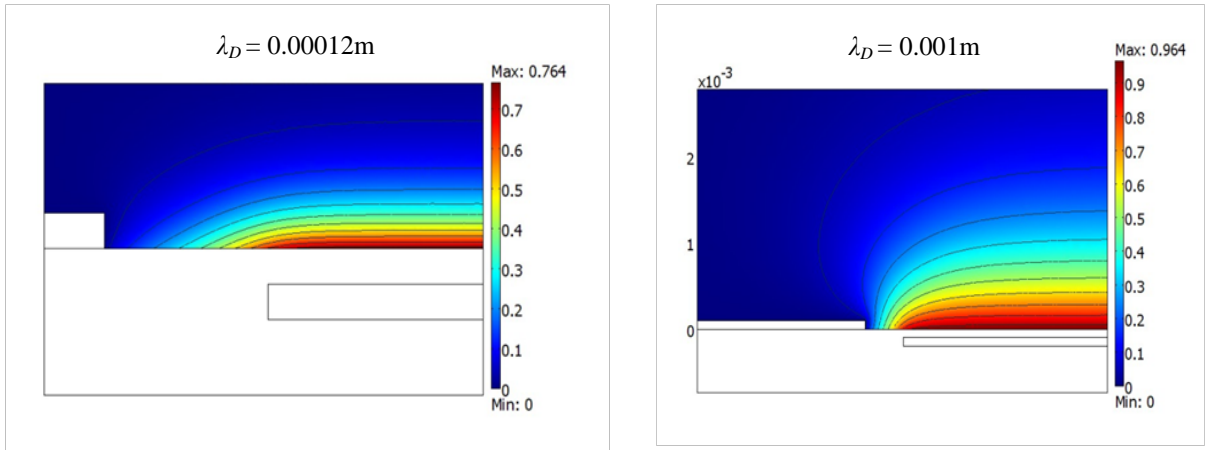


Figure 15: Non-dimensionalised charged density propagation with increased $\lambda_D = 0.00012$ m and $\lambda_D = 0.001$ m.

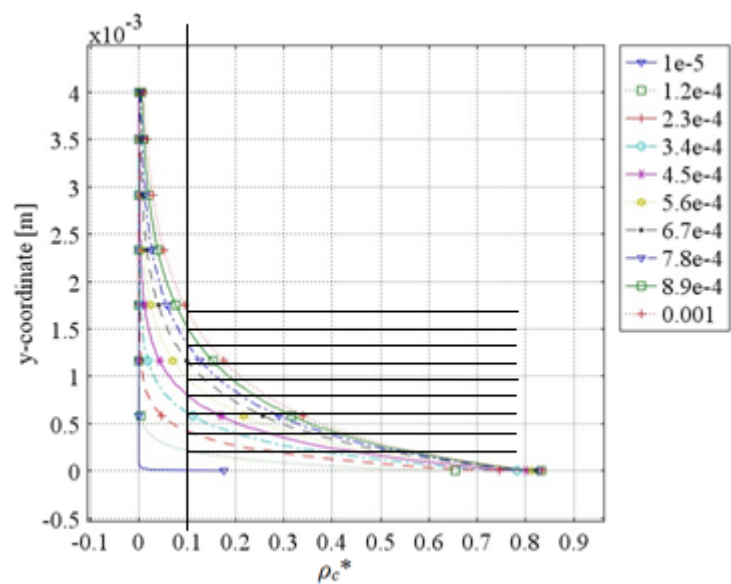


Figure 16: Linear increments of the Debye length and the resulting non-dimensionalised charged density distribution.

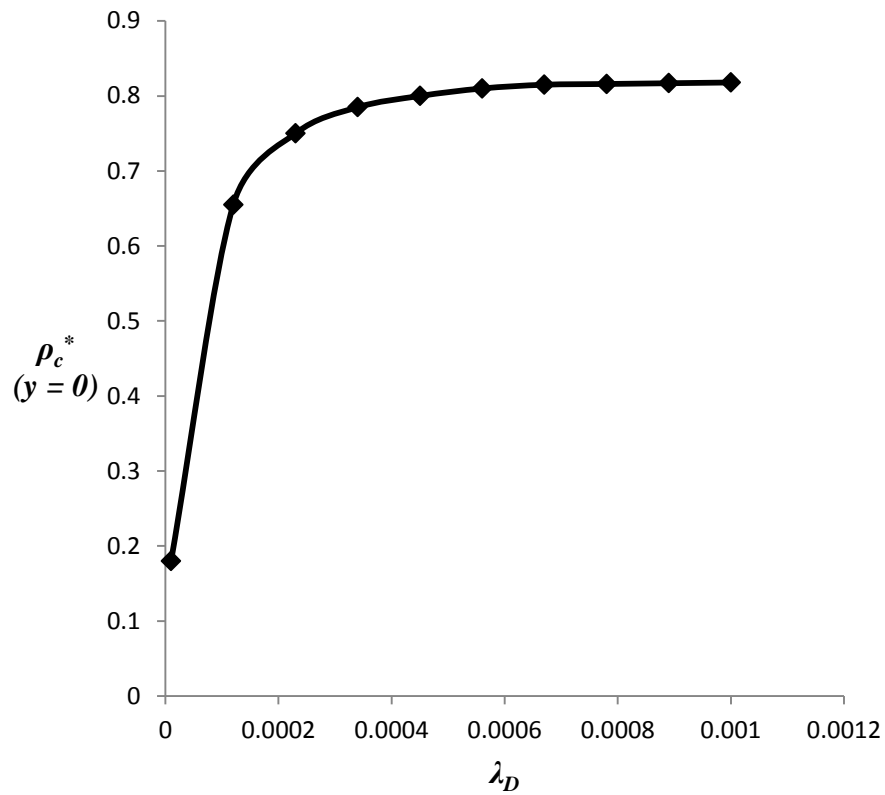


Figure 17: Nonlinear relationship between ρ_c^* and λ_D at $y = 0$.

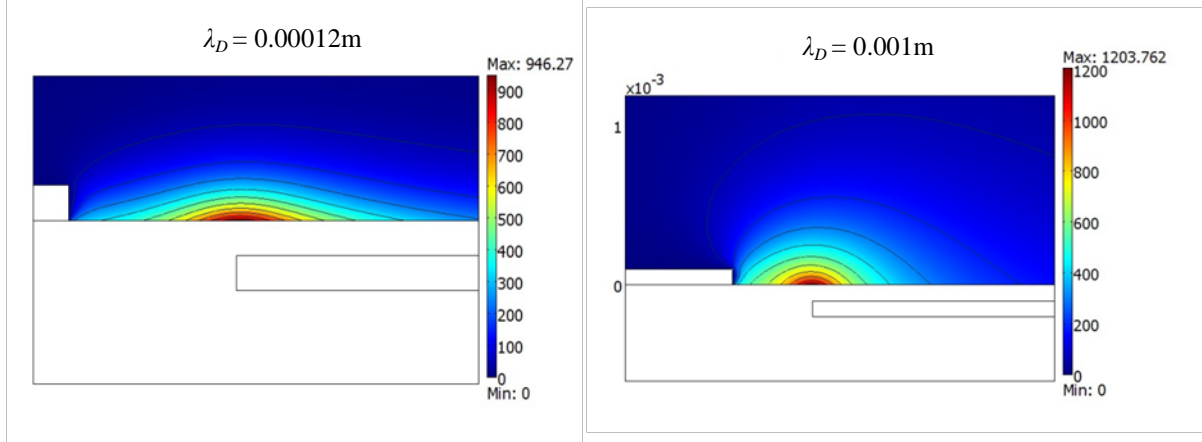


Figure 18: Non-dimensionalised body force propagation when $\lambda_D = 0.00012$ and $\lambda_D = 0.001$ m.

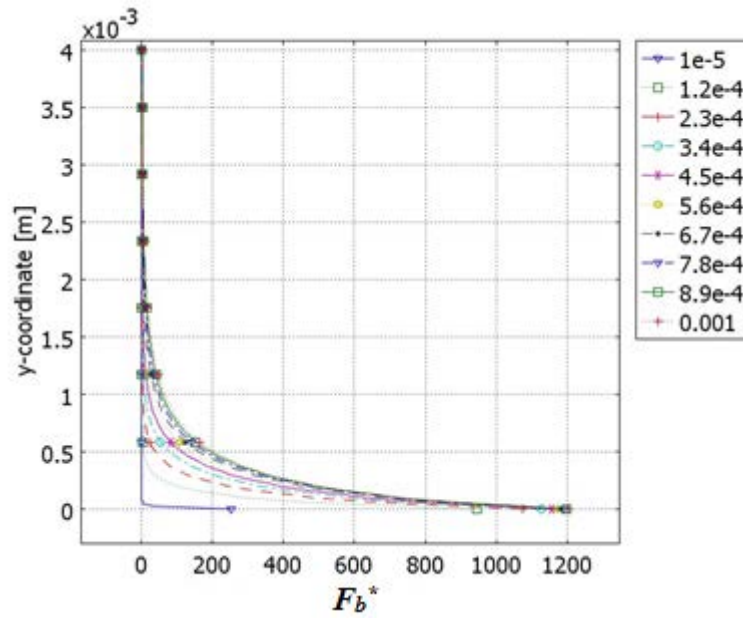


Figure 19: Linear increments of the Debye length and the resulting non-dimensionalised body force distribution.

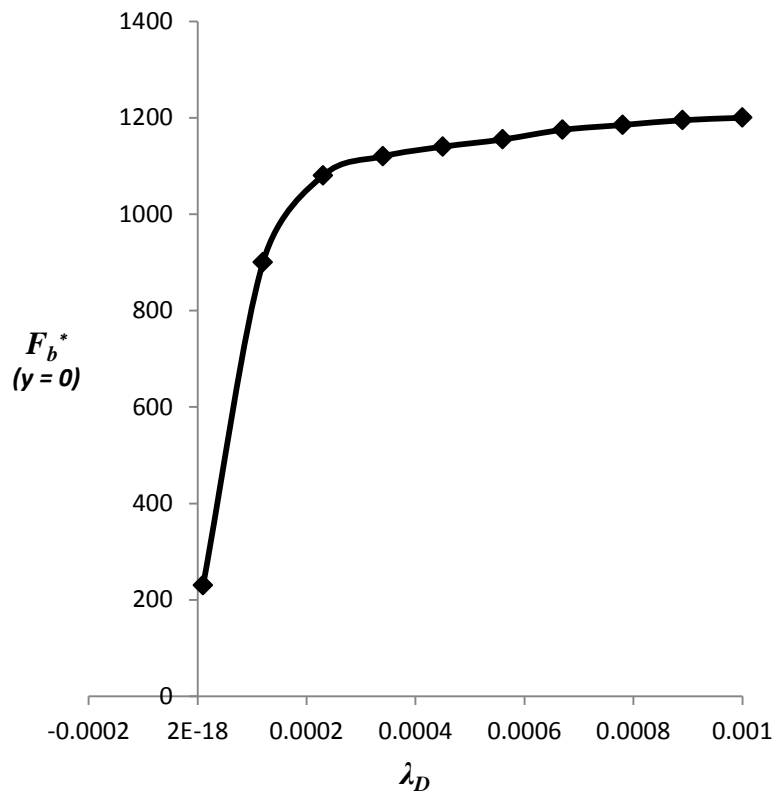


Figure 20: Nonlinear relationship between F_b^* and λ_D at $y = 0$.

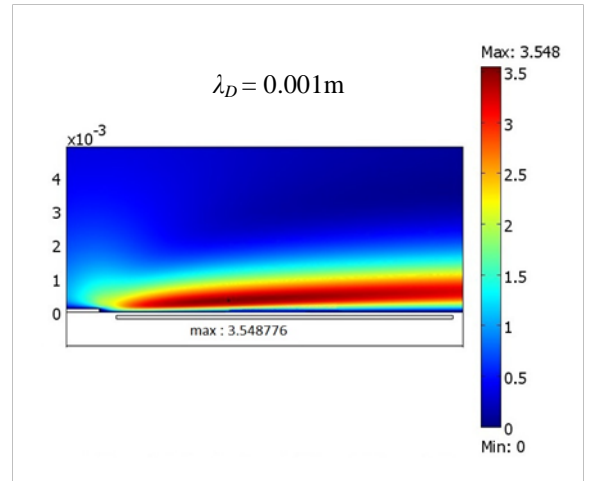
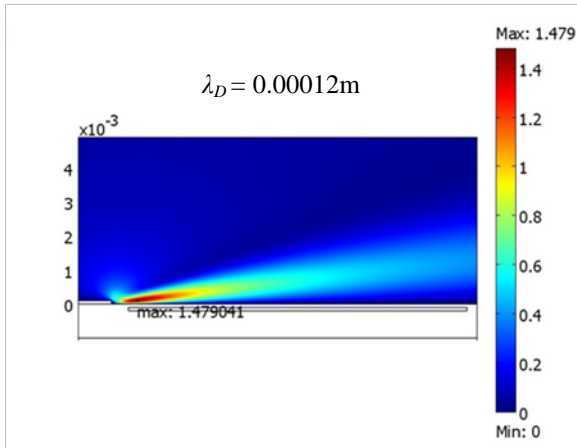


Figure 21: Induced velocity when $\lambda_D = 0.00012\text{ m}$ and $\lambda_D = 0.001\text{ m}$.

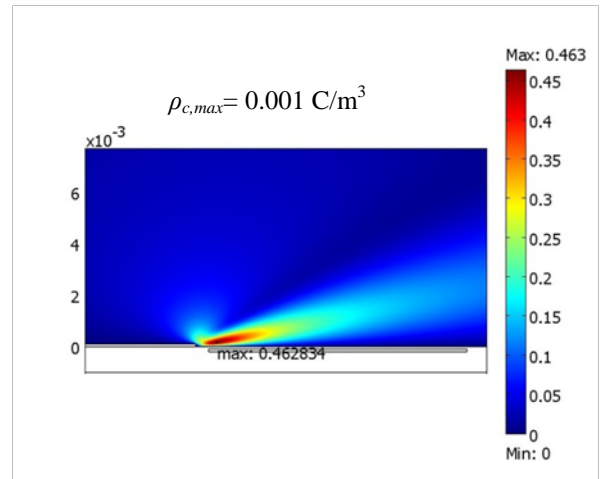
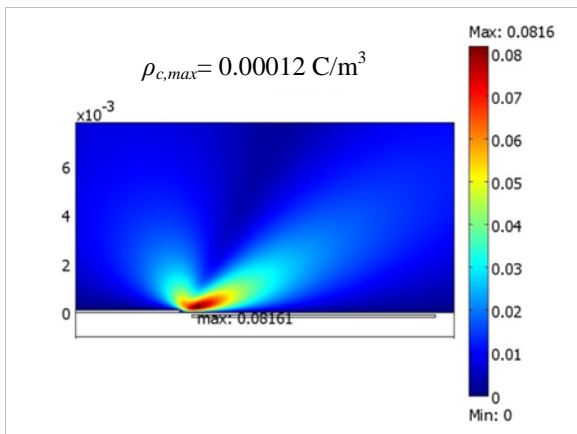


Figure 22: Induced velocity profiles propagations when $\rho_{c,max} = 0.00012\text{ C/m}^3$ and $\rho_{c,max} = 0.001\text{ C/m}^3$.

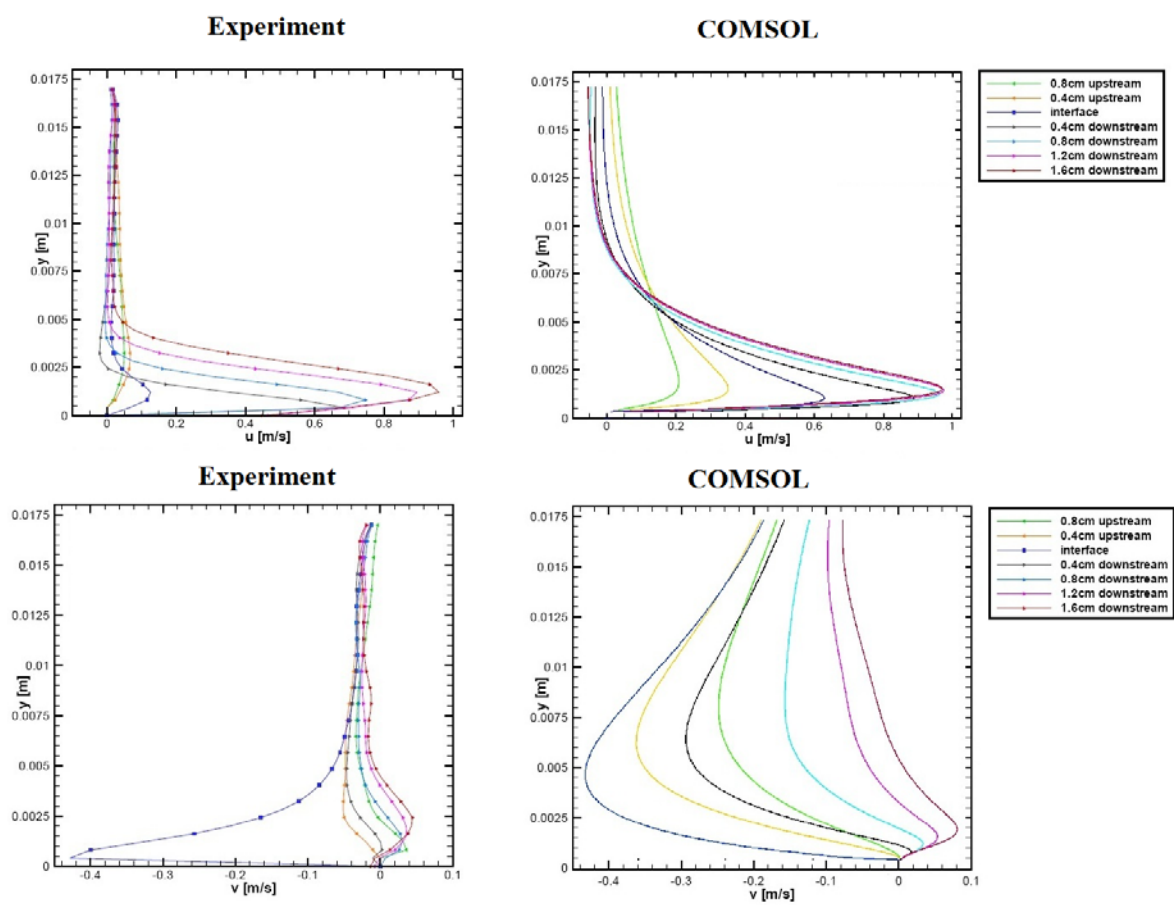


Figure 23 The u - (left) and v -velocity (right) profiles for the tuned parameters of the Debye length and maximum charged density compared with experimental results.